Geophysical Prospecting

EAGE EUROPEAN ASSOCIATION OF GEOSCIENTISTS & ENGINEERS

Geophysical Prospecting, 2015, **63**, 243–255 doi: 10.1111/1365-2478.12185

Sharp spatially constrained inversion with applications to transient electromagnetic data

Giulio Vignoli[1]*, Gianluca Fiandaca[2], Anders Vest Christiansen[2], Casper Kirkegaard[2] and Esben Auken[2]

[1]*Geological Survey of Denmark and Greenland, 8270 Højbjerg, Denmark, and* [2]*Hydrogeophysics Group, Department of Geoscience, Aarhus University, 8000 Aarhus, Denmark*

Received April 2013, revision accepted May 2014

ABSTRACT

Time-domain electromagnetic data are conveniently inverted by using smoothly varying 1D models with fixed vertical discretization. The vertical smoothness of the obtained models stems from the application of Occam-type regularization constraints, which are meant to address the ill-posedness of the problem. An important side effect of such regularization, however, is that horizontal layer boundaries can no longer be accurately reproduced as the model is required to be smooth. This issue can be overcome by inverting for fewer layers with variable thicknesses; nevertheless, to decide on a particular and constant number of layers for the parameterization of a large survey inversion can be equally problematic.

Here, we present a focusing regularization technique to obtain the best of both methodologies. The new focusing approach allows for accurate reconstruction of resistivity distributions using a fixed vertical discretization while preserving the capability to reproduce horizontal boundaries. The formulation is flexible and can be coupled with traditional lateral/spatial smoothness constraints in order to resolve interfaces in stratified soils with no additional hypothesis about the number of layers. The method relies on minimizing the number of layers of non-vanishing resistivity gradient, instead of minimizing the norm of the model variation itself. This approach ensures that the results are consistent with the measured data while favouring, at the same time, the retrieval of horizontal abrupt changes. In addition, the focusing regularization can also be applied in the horizontal direction in order to promote the reconstruction of lateral boundaries such as faults.

We present the theoretical framework of our regularization methodology and illustrate its capabilities by means of both synthetic and field data sets. We further demonstrate how the concept has been integrated in our existing spatially constrained inversion formalism and show its application to large-scale time-domain electromagnetic data inversions.

Key words: Spatially constrained inversion, Lateral discontinuities, Sharp boundaries, Focusing inversion, (Airborne) time-domain EM.

1. INTRODUCTION

Transient electromagnetic (TEM) surveying is a well-established geophysical discipline with applications ranging

*Giulio Vignoli was formerly at: Hydrogeophysics Group Aarhus University, Department of Geoscience, 8000 Aarhus, Denmark. E-mail: gv@geus.dk

from mineral exploration to groundwater and geological mapping. A main characteristic of the method is its ability to collect (particularly during airborne surveys) extremely large data sets that can be very time-consuming to process and invert. Full 3D inversion is possible but is typically impractical due to the size of the surveys. The fact that Maxwell's equations have to be solved for each transmitter location makes the rigorous 3D inversion (e.g., Sasaki 2001, 2003) particularly time-consuming. Attempts of fast and effective 2D/3D inversion schemes based on approximations have been recently developed and applied to TEM data (Wilson, Raiche, and Sugeng 2006; Guillemoteau, Sailhac, and Behaegel 2012). With the advent of powerful and inexpensive parallel computers, finite-volume (Haber, Oldenburg, and Shekhtman 2007; Yang and Oldenburg 2012), finite-difference (Newman and Commer 2005), and integral equation (Cox, Wilson, and Zhdanov 2010) techniques are also becoming increasingly popular and appealing. Up to date, however, 3D inversion is still not a routine practice, and for many target settings, the benefits of current 3D methods over 1D are debatable (Viezzoli *et al.* 2010).

Comprehensive TEM inversion codes based on 1D forward modelling typically use lateral/spatial constraints to regularize the inversion and obtain solutions that are in accordance with the expected geological variations (Christensen and Tølbøll 2009; Vallée and Smith 2009; Brodie 2010). This approach of inverting for pseudo-2D/3D models using local 1D models entangled by constraints has proven very effective in modelling quasi-layered structures where 2D/3D effects are not too pronounced (Newman, Anderson, and Hohmann 1987; Sengpiel and Siemon 2000; Auken *et al.* 2005). Most algorithms falling within this category offer support for two types of modelling: "discrete model" inversion that inverts for a limited number of layers with variable layer boundaries and inversion for "smooth models" based on a large number of stacked layers with fixed vertical discretization. In the latter case, the inversion problem is typically highly underdetermined, making vertical regularization necessary to stabilize the solution (Constable, Parker, and Constable 1987). In the former strategy, the inversion can operate without any additional (vertical) regularization due to its much lower number of free model parameters. Both approaches have their trade-offs as the smooth one produces sections where formation boundaries are smeared out by regularization, whereas the discrete approach can introduce artefacts in case of unexpectedly complex geology. The discrete model technique is also more sensitive to the specific choice of starting model, and for these reasons, both types of inversions are typically used as complementary solutions.

Here, we describe and demonstrate a novel algorithm that implements an extension of the pseudo-3D spatially constrained inversion (SCI) formalism (Viezzoli *et al.* 2008) and its pseudo-2D special case known as laterally constrained inversion (LCI) (Auken and Christiansen 2004). The extension consists of a new regularizing term that is not derived from the L_2 norm of the spatial gradient of the solution but rather depends on its support (Portniaguine and Zhdanov 1999; Zhdanov and Tolstaya 2004; Pagliara and Vignoli 2006; Zhdanov, Vignoli, and Ueda 2006; Blaschek, Hördt, and Kemna 2008; Vignoli, Cassiani, and Deiana 2012). Specifically, we base our new algorithm on the gradient support regularization and refer to the complete scheme as sharp SCI (sSCI). The introduction of the new regularization term promotes solutions that are both compatible with the observed data and, at the same time, features a minimum number of spatial (vertical and/or lateral) model variations. By using this technique, we essentially eliminate the need for consulting both discrete and smooth inversions.

2. METHODOLOGY

In the framework of Tikhonov regularization theory (Tikhonov and Arsenin 1977), *a priori* information is included in the inversion process and formalized via regularizing terms. Instead of simply minimizing the distance (usually defined by the L_2 norm) between the observed and calculated data, the regularized objective functional incorporates additional stabilizing terms. Hence, the solution minimizing the full objective functional is compatible with both the observed data and any assumptions about the investigated physical system enforced by means of the stabilizer. Including *a priori* information turns the originally ill-posed problem into a well-posed one, where the solution is unique and stable with respect to the data.

Here, we are interested in incorporating the assumption that sharp resistivity contrasts exist between different lithologies in the investigated subsoil. Currently, the most widely used stabilizers are smoothing functionals that constrain the spatial variation of the sought parameter field (Constable *et al.* 1987), which is exactly the kind of regularization employed in the standard SCI algorithm. In the SCI, the parameters of neighbouring 1D models are entangled by means of such smooth regularization terms, essentially constraining (and smoothing) the amount of lateral variation of the model parameters. The SCI scheme further employs vertical

regularization on each individual 1D model in the case of inversion for smooth models. With the sSCI formalism, our goal is to resolve sharp layer boundaries by using the minimum gradient support (MGS) regularization. We investigate the application of the MGS, along the vertical direction, to be able to reconstruct subhorizontal interfaces (potentially eliminating the need for discrete inversion that makes unwanted assumptions about the ground layering). We also study the use of the sSCI approach along the horizontal direction to effectively resolve lateral discontinuities (e.g., due to faults or blocky mineral inclusions).

2.1 Algorithm: from spatially constrained to sharp spatially constrained inversion

Spatially and laterally constrained 1D inversion techniques have been successfully applied to many different kinds of data, including vertical electrical soundings (Auken and Christiansen 2004; Auken *et al.* 2005), seismic surface wave (Wisén and Christiansen 2005), TEM (Auken *et al.* 2008; Viezzoli *et al.* 2008), frequency-domain electromagnetics (Monteiro Santos 2004; Brodie and Sambridge 2006; Triantafilis and Monteiro Santos 2009), magnetic resonance soundings (Behroozmand *et al.* 2012b), and time-domain induced polarization (Fiandaca *et al.* 2012, 2013). For simplicity, we consider the special case of SCI inversion of TEM data. In this case, the vectors in the data and in the model space, respectively, become

$$\mathbf{d} = [\log(\rho_{a1}), \log(\rho_{a2}), \log(\rho_{a3}), \ldots, \log(\rho_{aN})]^T, \tag{1}$$

and

$$\mathbf{m} = [\mathbf{m}_1, \mathbf{m}_2, \mathbf{m}_3, \ldots, \mathbf{m}_{n_x}]^T. \tag{2}$$

In these equations, $\rho_{ai}, i = 1, \ldots, N$ denotes the apparent resistivity data collected along a profile and for different time gates, and each $\mathbf{m}_j$, $j = 1, \ldots, n_x$ is the vector of the n_ℓ resistivities and the $(n_\ell - 1)$ thicknesses at the jth sounding position: $\mathbf{m}_j = [\log(\rho_{j1}), \ldots, \log(\rho_{jn_\ell}), \log(t_{j1}), \ldots, \log(t_{j(n_\ell-1)})]^T$.

Thus, the estimated solution is the minimizer of the summation between the data misfit

$$\phi(\mathbf{m}) = \left\| \mathbf{Q}_d(\mathbf{d}_{obs} - g(\mathbf{m})) \right\|_{L_2}^2 \tag{3}$$

and the stabilizer terms

$$s(\mathbf{m}) = \left\| \boldsymbol{\beta}^{-1} \mathbf{Q}_p \, \mathbf{R}_p \, \mathbf{m} \right\|_{L_2}^2, \tag{4}$$

where g is the nonlinear mapping relating the model to the data space, $\mathbf{R}_p$ is the roughness operator providing the specifics of the regularization, and $\boldsymbol{\beta}^{-1}$ consists of a diagonal matrix of weights controlling the relative importance between the data and the stabilizer. Finally, $\mathbf{Q}_p$ and $\mathbf{Q}_d$ are simple weighting matrices in the model and data space, respectively. In the data case, $\mathbf{Q}_d$ typically weights the data residuals by the inverse of the uncertainty in the data, i.e.,

$$(\mathbf{Q}_d)_{ii} = \delta_i^{-1}. \tag{5}$$

In the original LCI/SCI schemes (e.g., Auken and Christiansen 2004; Viezzoli *et al.* 2008), the roughness matrix $\mathbf{R}_p$ is implemented as a linear difference operator and the entries of the diagonal $\boldsymbol{\beta}$ matrix are all set to unity; in the case of $\mathbf{Q}_p$, the entries $(\mathbf{Q}_p)_{kk} = \sigma_k^{-1}$ are inversely proportional to the model variance σ_k and specify the different degrees of variability associated with the spatial constraints.

In the SCI implementation, the non-linear objective function is minimized by using the Levenberg–Marquart algorithm, providing a solution by iterating over n:

$$\mathbf{m}_{n+1}^{(\mathrm{SCI})} = \mathbf{m}_n^{(\mathrm{SCI})} + \left\{ \begin{array}{l} \left[\mathbf{G}_n^T \mathbf{C}_{obs}^{-1} \mathbf{G}_n + \beta^{-1} \mathbf{R}_p^T \mathbf{C}_c^{-1} \mathbf{R}_p + \lambda \mathbf{I} \right]^{-1} \cdot \\ \left[\mathbf{G}_n^T \mathbf{C}_{obs}^{-1} \left(\mathbf{d}_{obs} - \mathrm{g}(\mathbf{m}_n^{(\mathrm{SCI})}) \right) + \beta^{-1} \mathbf{R}_p^T \mathbf{C}_c^{-1} \left(-\mathbf{R}_p \mathbf{m}_n^{(\mathrm{SCI})} \right) \right] \end{array} \right\}, \tag{6}$$

where G_n is the Jacobian matrix of the nonlinear mapping g; $\mathrm{C}_{obs}^{-1} = \mathrm{Q}_d^T \mathrm{Q}_d$ is a covariance matrix specifying the data uncertainties, whereas $\mathrm{C}_c^{-1} = \mathrm{Q}_p^T \mathrm{Q}_p$ defines the strength of the regularizing constraints; and λ is simply a Marquart damping parameter that is iteratively updated to stabilize the minimization process (Marquart 1963).

The reason of the SCI smoothness is clear if we rewrite equation (4) in a more explicit way:

$$s^{(SCI)}(\mathbf{m}) = \frac{1}{\beta} \sum\nolimits_k \frac{(\mathbf{R}_p \mathbf{m})_k^2}{\sigma_k^2}. \tag{7}$$

In minimizing the stabilizer, the contribution $(\mathbf{R}_p \mathbf{m})_k^2 / \sigma_k^2$ of the kth term (which will be referred to as "penalization" term) is proportional to the square of the value of the variation of the kth component of $\mathbf{m}$. This linear relationship is illustrated with a straight line in Fig. 1, which clearly shows that an increase in model parameter variation will always lead to greater penalization in the stabilizer. This intrinsic property of the minimum L_2 norm methodology essentially prevents reconstruction of blocky features since this requires an upper limit on the degree of penalization regardless of variation magnitude. This can be overcome by using the sSCI

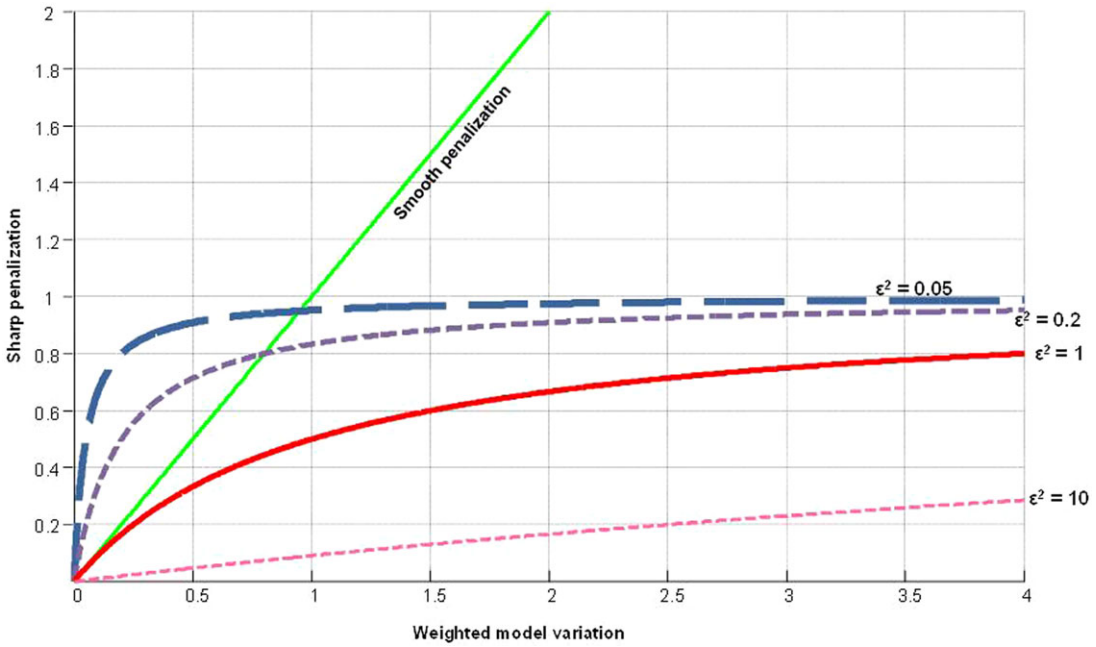

Figure 1 Sharp penalization $(\frac{(\mathbf{R}_p\mathbf{m})_k}{\sigma_k})^2 / [(\frac{(\mathbf{R}_p\mathbf{m})_k}{\sigma_k})^2 + \varepsilon^2]$ plotted against the weighted variation of the model $(\frac{(\mathbf{R}_p\mathbf{m})_k}{\sigma_k})^2$ for different values of the focusing parameter ε^2. For comparison, the smooth penalization $(\frac{(\mathbf{R}_p\mathbf{m})_k}{\sigma_k})^2$ is also shown (solid green line).

scheme; the full expression for the corresponding stabilizer is

$$s^{(sSCI)}(\mathbf{m}) = \sum_k \frac{1}{\beta_k} \frac{\left(\frac{(\mathbf{R}_p\mathbf{m})_k}{\sigma_k}\right)^2}{\left(\frac{(\mathbf{R}_p\mathbf{m})_k}{\sigma_k}\right)^2 + \varepsilon^2}, \tag{8}$$

and is discussed in the following.

Within the formalism of the sSCI, we use the model variance σ_k as a tuneable threshold controlling the sharpness of the inversion while we keep the ε parameter constant. To explain the reasoning behind this, we first discuss how we select the value for ε from the plot in Fig. 1 showing the variability of the sSCI penalization as a function of the weighted model variation for different ε^2 values. When $\varepsilon^2 = 1$, σ_k acts as a loosely defined threshold: model variations with $(\frac{(\mathbf{R}_p\mathbf{m})_k}{\sigma_k})^2 < 1$ are weakly penalized, whereas model variations above σ_k can never contribute with a penalization larger than one. Hence, by using an MGS stabilizer with $\varepsilon^2 = 1$, we penalize only the number of variations larger than the threshold, rather than the magnitude of the variation itself. Moreover, the use of $\varepsilon^2 = 1$ provides the benefit of obtaining similar behaviour for the MGS stabilizer and the L_2 norm stabilizer for small values of $(\mathbf{R}_p\mathbf{m})_k^2/\sigma_k^2$ (Fig. 1). This allows for reconstruction of sharp boundary targets while maintaining the effect of smoothing regularization for small model parameter variations. By selecting too small ε^2 values (in Fig. 1, $\varepsilon^2 = 0.05$ and 0.02), we basically apply the same maximum penalization to every model characterized by a variation different from zero. This would result in a very oscillating solution since it does not really matter if the variation is large or small as long as it is non-zero. On the contrary, if a large ε^2 value (e.g., $\varepsilon^2 = 10$) is used, a penalization nearly proportional to the model variation is applied. In this case, the regularization will not lead to the desired blocky solution.

Thus, σ_k defines the threshold where a model parameter variation is considered large enough to be penalized (i.e., it is large enough to contribute to the focusing MGS stabilizer in equation (8) and Fig. 1). In other words, σ_k and the corresponding $\mathbf{C}_c$ entries define the level of homogeneity in each reconstructed sub-volume and the level of (non-penalized) variability within each individual area. Basically, by setting σ_k equal to, for example, 1.04, the MGS stabilizer considers all resistivity changes larger than 4% as possible variations in structure, whereas variability within 4% is treated as homogeneous.

Concerning the diagonal matrix $\boldsymbol{\beta}$, we use only two distinct values for its entries. One value for the entries in equation (8) involves the vertical variation and another is used for the horizontal components. In general, the $\boldsymbol{\beta}$ matrix elements control the balance between data misfit and

regularization; therefore, they should be chosen to fit the data to an appropriate degree. For the sSCI, however, the use of two distinct values for $\boldsymbol{\beta}$ extends its functionality to further control the ratio between horizontal and vertical focusing strengths. In the following, for the sSCI, we set the two $\boldsymbol{\beta}$ component values to 15 normalized by the number of lateral and vertical constraints per 1D model, respectively. We choose these values on the basis of a large number of numerical experiments that demonstrate these numbers to be robust and capable of guaranteeing a satisfactory data fit. In general, by selecting smaller values for $\boldsymbol{\beta}$, we could obtain more blocky solution but without achieving the desired data misfit. On the other hand, too large $\boldsymbol{\beta}$ component values led to smoother solutions.

The integration of the novel sSCI regularization into the existing SCI minimization scheme is straightforward since the smoothing functional in equation (7) uses the L_2 norm of the model variation $\mathbf{R}_p\mathbf{m}$ and the only difference with the sharp functional in equation (8) is in the weighting matrix. In the former case, the weighting matrix is the diagonal matrix of the model variances $\mathbf{Q}_p$, whereas in the latter, the weighting matrix simply becomes: $\mathbf{W}_\varepsilon\mathbf{Q}_p\mathbf{R}_p$, where $\mathbf{W}_\varepsilon$ is a diagonal matrix with non-zero elements equal to

$$(\mathbf{W}_\varepsilon)_k = \frac{1}{\sqrt{(\mathbf{Q}_p\mathbf{R}_p\mathbf{m})_k^2 + \varepsilon^2}}. \tag{9}$$

Consistently, the stabilizer expression (equation (6)) turns into $s^{(sSCI)}(\mathbf{m}) = \left\|\boldsymbol{\beta}^{-1}\mathbf{W}_\varepsilon\mathbf{Q}_p\mathbf{R}_p\mathbf{m}\right\|_{L_2}^2 = \left\|\boldsymbol{\beta}^{-1}\mathbf{Q}_p\mathbf{H}_\varepsilon\mathbf{m}\right\|_{L_2}^2$. From the definition of $\mathbf{W}_\varepsilon$, we see that the introduction of the sharp MGS stabilizer has made the weighting matrix elements model dependent (Vignoli *et al.* 2012). In principle, in the expression for the iterative model update, terms containing the Fréchet derivative of $\mathbf{W}_\varepsilon$ with respect to $\mathbf{m}$ should be included. Examples of inversion algorithm based on the minimum support stabilizer, taking into account these terms, are described in Zhdanov *et al.* (2006) and Vignoli *et al.* (2012). However, since we wanted to implement a focusing algorithm by introducing the minimum number of modifications with respect to the original SCI scheme, we disregard those terms and use instead a reweighting strategy taking into account simply the terms with $\mathbf{W}_\varepsilon$. Thus, the variable weighting matrix $\mathbf{W}_\varepsilon$ is recomputed on each iteration $\mathbf{W}_\varepsilon = \mathbf{W}_\varepsilon^{(n)} = \mathbf{W}_\varepsilon(\mathbf{m}_n)$ based on the $\mathbf{m}_n$ from the previous iteration, whereas the contributions of the terms accounting for the derivative of $\mathbf{W}_\varepsilon$ are neglected. This simplified approach leads to an iterative model update expression for the sSCI that is extremely close to equation (6) concerning the SCI:

$$\mathbf{m}_{n+1}^{(sSCI)} = \mathbf{m}_n^{(sSCI)} + \left\{ \begin{array}{l} \left[\mathbf{G}_n^T\mathbf{C}_{obs}^{-1}\mathbf{G}_n + \boldsymbol{\beta}^{-1}(\mathbf{H}_\varepsilon^{(n)})^{\mathrm{T}}\mathbf{C}_c^{-1}\mathbf{H}_\varepsilon^{(n)} + \lambda\mathbf{I}\right]^{-1} \cdot \\ \left[\mathbf{G}_n^T\mathbf{C}_{obs}^{-1}\left(\mathbf{d}_{obs} - \mathrm{g}(\mathbf{m}_n^{(sSCI)})\right) + \boldsymbol{\beta}^{-1}(\mathbf{H}_\varepsilon^{(n)})^{\mathrm{T}}\mathbf{C}_c^{-1}\left(-\mathbf{H}_\varepsilon^{(n)}\mathbf{m}_n^{(sSCI)}\right)\right] \end{array} \right\}. \tag{10}$$

Hence, the inversion algorithm for the sSCI is the same as for the SCI after substituting the (constant) roughness operator $\mathbf{R}_p$ with the matrix (updated iteration by iteration) $\mathbf{H}_\varepsilon^{(n)}$.

In principle, neglecting the terms containing the $\mathbf{W}_\varepsilon$ derivative could lead to convergence issues in the minimization; however, we have experienced no problem in practice. For the reweighted optimization used here, the convergence rate depends on how accurate the (pseudo-quadratic) approximation of the weighting matrix $\mathbf{H}_\varepsilon^{(n)}$ is with respect to the original (non-quadratic) norm (Zhdanov 2002). Across all of our numerical experiments, we find that the convergence rate of the SCI algorithm remains essentially the same even after adding the sSCI term.

3. SYNTHETIC DATA

We demonstrate the application of the new algorithm by using two synthetic examples. In particular, we compare the capabilities of the sSCI in reproducing layer boundaries against the smooth and discrete SCI inversions. The goals are to assess whether sSCI can be adopted as a valid alternative to discrete inversions and understand the differences between sSCI and traditional smooth SCI.

The considered synthetic models are representative of typical glacial buried valleys. Buried valleys are complex structures filled with glaciolacustric clay, till, meltwater sand, and gravel and provide classical targets for hydrogeophysical surveys. The presented models mimic the geology studied in Jørgensen *et al.* (2012), whereas the details of the generation of the synthetic 3D TEM data by using the TEMDDD code (Árnason 2008) are the same as discussed by Auken *et al.* (2008). Both synthetic models are characterized by a 3D resistivity distribution; in fact, the top layer of the model represents a soil of randomly generated resistivity varying both along and perpendicularly to the profile. Located beneath the top layer, we find the actual 2D buried valley structures. The synthetic data extracted from the models simulate a ground-based TEM instrument, transmitting a current of 3 A in a 40 m × 40 m square loop. The soundings are measured every 20 m, and the corresponding data are perturbed by noise consisting of: (i) Gaussian 2% contribution and (ii) "background"

contribution characterized by a $t^{-1/2}$ trend with a value of 3 nV/m^2 at 1 ms (Auken *et al.* 2008). After adding the noise perturbation, the synthetic data were processed as any field data set, resulting in an uneven number of gates per sounding and varying error bars. For the inversion, a 50-Ωm uniform half-space was used as a starting model, whereas the vertical discretization is characterized by logarithmically increasing layer thicknesses. Spatial regularization was applied using constant setting throughout all inversions and applied to the resistivity values. For the smooth horizontal regularization, a constraint factor of 1.2 was used to entangle the resistivities of neighbouring model layers, whereas for the vertical direction, a factor of 2.0 was applied. As the inversion is performed in logarithmic model space, these values essentially amount to assigning a variance of ∼20% on the resistivities of horizontally neighbouring layers and a variance of ∼100% in the vertical direction. For the sSCI, we use the global constant settings presented in the previous section, with $\sigma_k = 1.04$ and $\sigma_m = 1.12$ (here, the k and m indexes are, respectively, spanning the $\mathbf{C}_c$ components concerning the horizontal and vertical constraints). Thus, by using these values, the regularization essentially considers an area homogeneous if the horizontal and vertical variations are smaller than 4% and 12%, respectively.

3.1 Model A

The first discussed synthetic model is shown in Fig. 2. It represents a relatively simple valley (Fig. 2(a)) incised into thick clays (5 Ωm) and filled by sands (100 Ωm) below the groundwater table. The valley has 26° sloping flanks with the bottom situated at a depth of 150 m. The top layer is inhomogeneous with a log-normal resistivity distribution having a mean value of 40 Ωm for the left side (clay–till) and 400 Ωm for the right side (dry quaternary sand).

Comparing the final inversion model, we find the 16-layer smooth SCI result (Fig. 2(b)) to retrieve reasonably well the main features of the true model: the mean resistivity value of the top layer is well reconstructed on both sides, the resistivity of the valley is slightly overestimated (particularly on the left side), and the flanks appear less steep than they actually are due to the presence of a smooth (artificial) transition between the (overestimated) high resistivity inside the valley and the conductive clay.

Figure 2(c) shows that the quality of the final inversion improves when the MGS constraints are applied along the vertical direction, and the regular SCI smoothing is kept acting laterally. The resistivity level of the valley fill is now slightly better determined and also more homogeneously reproduced (even if the resistivity of the left side of the valley is still higher than the true value). The boundary at the interface between the first layer and the valley is more precisely retrieved. For example, the artificial horizontal transition at the bottom of the first layer, on the right side, introduced by the smooth inversion (Fig. 2(b)) has been almost completely removed by the vertical sharp algorithm (Fig. 2(c)).

The sSCI using MGS constraints in both the vertical and horizontal directions (Fig. 2(d)) further improves the result. Not only the actual locations of the abrupt resistivity changes in the true model are more accurately mapped (e.g., the interface between the first layer and the sandy valley along the entire section is precisely located) but the true resistivity values are also more correctly recovered. For example, the sand's homogeneous resistivity is very well inferred almost to the depth of investigation (DOI) (Christiansen and Auken 2012). Clearly, the MGS algorithm enhances all the "sharp" features in the data, including the so-called "pant–leg" effect due to presence of an abrupt lateral change in conductivity. Hence, for example, the vertical boundary in the top layer results in a spurious conductive feature in the first few tens of metres in the valley fill. This artefact is present in all the reconstruction in Fig. 2 but is less fuzzy and more clearly detectable in the sharp reconstructions.

In Fig. 2(e), the data residuals of the three inversion schemes show that all the solutions fit the data comparably well. The only area where the sSCI misfit is significantly higher than the others is approximately located at the centre of the section where several sharp changes are present (the vertical one splitting the first layer into two parts and the horizontal interface at the top of the resistive valley). In that position, several non-zero terms are contributing to the summation (equation (8)) defining the sSCI stabilizer, and this hinders the data misfit minimization. In other words, the local higher data misfit results from the competition with the *a priori* information enforcement.

3.2 Model B

The second synthetic example (Fig. 3(a)) consists of two layers lying on a conductive half-space (5 Ωm). With respect to Model A, the top layer now consists of a single log-normal resistivity distribution with mean resistivity value equal to 40 Ωm across the whole area. The second layer has a 70-Ωm resistivity and is incised by a paleovalley. A 20-Ωm material is filling the right side base of the paleovalley that, everywhere

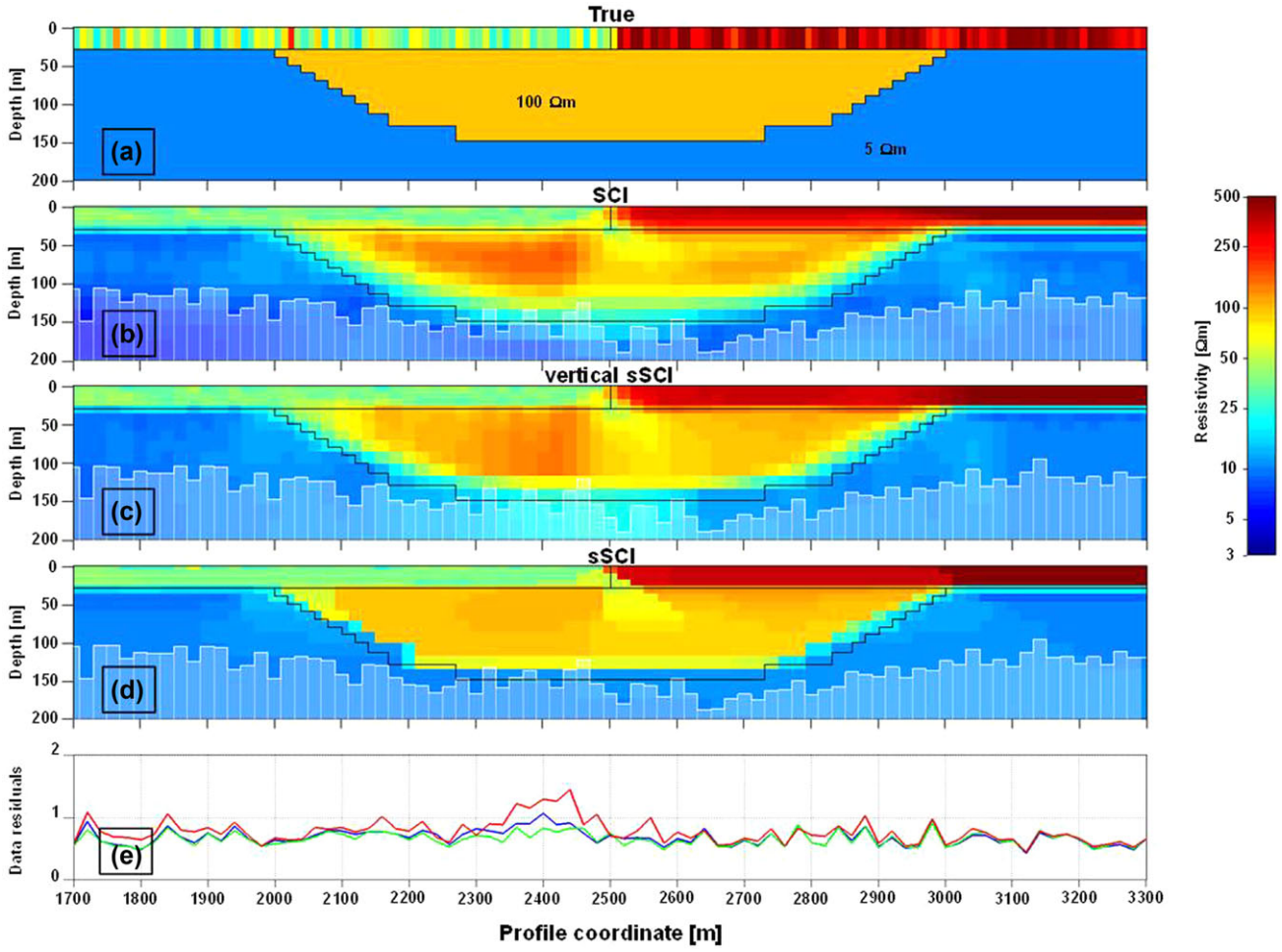

Figure 2 Model A. (a) True model. (b) SCI result (smooth constraints both in vertical and horizontal directions). (c) Vertical sSCI (laterally smooth and vertically sharp constraints). (d) sSCI (sharp constraints both in vertical and horizontal directions). (e) Data misfit: green, blue, and red lines show the residuals for the SCI, vertical sSCI, and multidirectional sSCI, respectively. The white-shaded area in (b)–(d) represents the DOI. Vertical exaggeration = 1.1x.

else, is characterized by a 100-Ωm resistivity. Comparing the inversion results, we again find that the standard smooth SCI is fairly successful in recovering the overall picture (Fig. 3(b)). If, instead of 16, only four layers are used for a laterally smooth SCI, the result in Fig. 3(c) is obtained. A four-layer parameterization has been chosen since the true model is characterized by four layers. In this inversion, no vertical constraints are connecting the resistivity values within each 1D model, and simply, the usual lateral smoothness is enforced ($\sigma_k = 1.2$). The most evident difference between Figs. 3(b) and (c) is in the higher precision of the few-layer inversion in locating the interfaces defining the resistive layers and the depth of the resistive valley. Also, the flanks of the conductive valley are better resolved since the few-layer parameterization reduces the smearing effect due to the smooth regularization. Similar to that in Fig. 3(b), the bottom of the conductive valley cannot be resolved since it is at the DOI limit.

In the case of sSCI utilizing vertical and horizontal MGS constraints (Fig. 3(d)), we again find that the reconstruction is significantly improved: the location of the interfaces is more accurate, and the overall resistivity levels are better recovered without overshooting the resistivity of the shallower valley. The result in Fig. 3(d) confirms that sSCI inherits, at the same time, the advantages of the multi-layer (regularized) inversion and the discrete (few-layer) reconstruction; thus, the sSCI allows retrieving the resistivity distributions by means of a fixed vertical discretization while preserving the capability to reproduce sharp features. In particular, the two 70-Ωm structures between depths of 30 m and 75 m are quite well retrieved both in terms of boundary location and resistivity value. Also

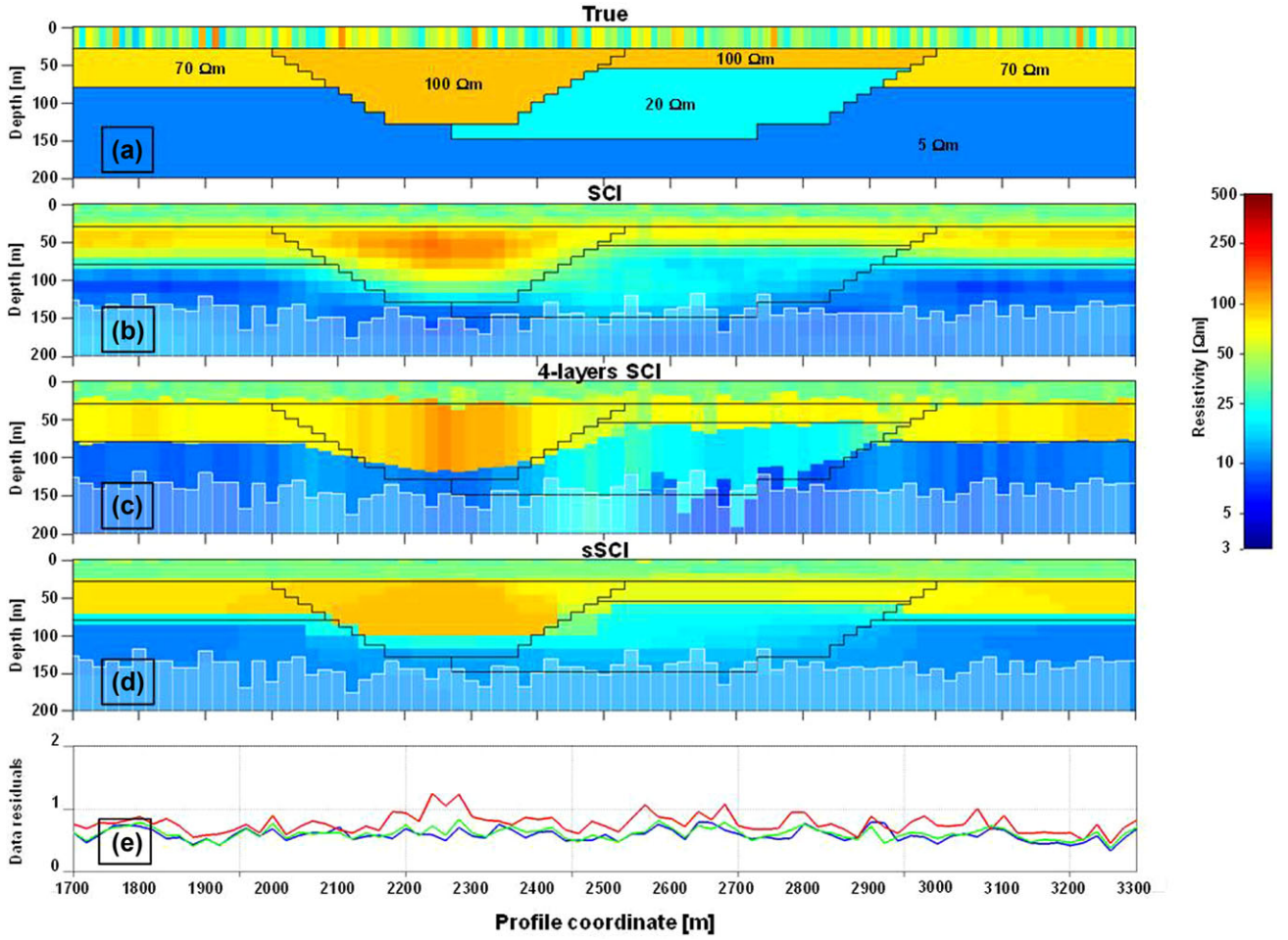

Figure 3 Model B. (a) True model. (b) SCI result (smooth constraints both in vertical and horizontal directions). (c) Discrete SCI (laterally smooth with a few-layer parameterization). (d) sSCI (sharp constraints both in vertical and horizontal directions). (e) Data misfit: green, blue, and red lines show the residuals for the multilayer SCI, few-layer SCI, and multilayer sSCI, respectively. The white-shaded area in (b)–(d) represents the DOI. Vertical exaggeration = 1.1x.

the geometry of the thin 100-Ωm layer on the right is reconstructed quite well by the sSCI, and the resistivity value is very close for all the inversion schemes (around 60 Ωm). In addition, the flanks of the resistive valley are reconstructed by the sSCI to a level comparable to the few-layer inversion quality.

Clearly, all the regularization schemes we have considered are designed to penalize, in different ways, the lateral resistivity variation. When the sensitivity of the physical method is not high enough, it might happen that the contribution from the stabilizing term is predominant. Hence, the information migrates from the areas better constrained by the data to the others. This explains why the bottom of the resistive valley embedded in a more conductive medium is hard to be correctly recovered and why, in all reconstructions, the valley base appears to be less resistive than in the true model. Of course, similar to the "pant–leg" effect in Model A, also for the Model B, when the sSCI algorithm is used, the regularization artefacts are sharper and therefore somewhat more pronounced. As for the Model A, the data misfit of the three solutions is comparable along the profile, and as expected, the sSCI residual is higher in correspondence of areas where several abrupt resistivity changes occur at the same time.

4. FIELD DATA

As part of the CLIWAT project (Harbo *et al.* 2011), airborne TEM data were collected near Tønder, in southern Denmark, in April 2009 (Fig. 4). The aim of the survey was to obtain a better understanding of the geological and hydrogeological

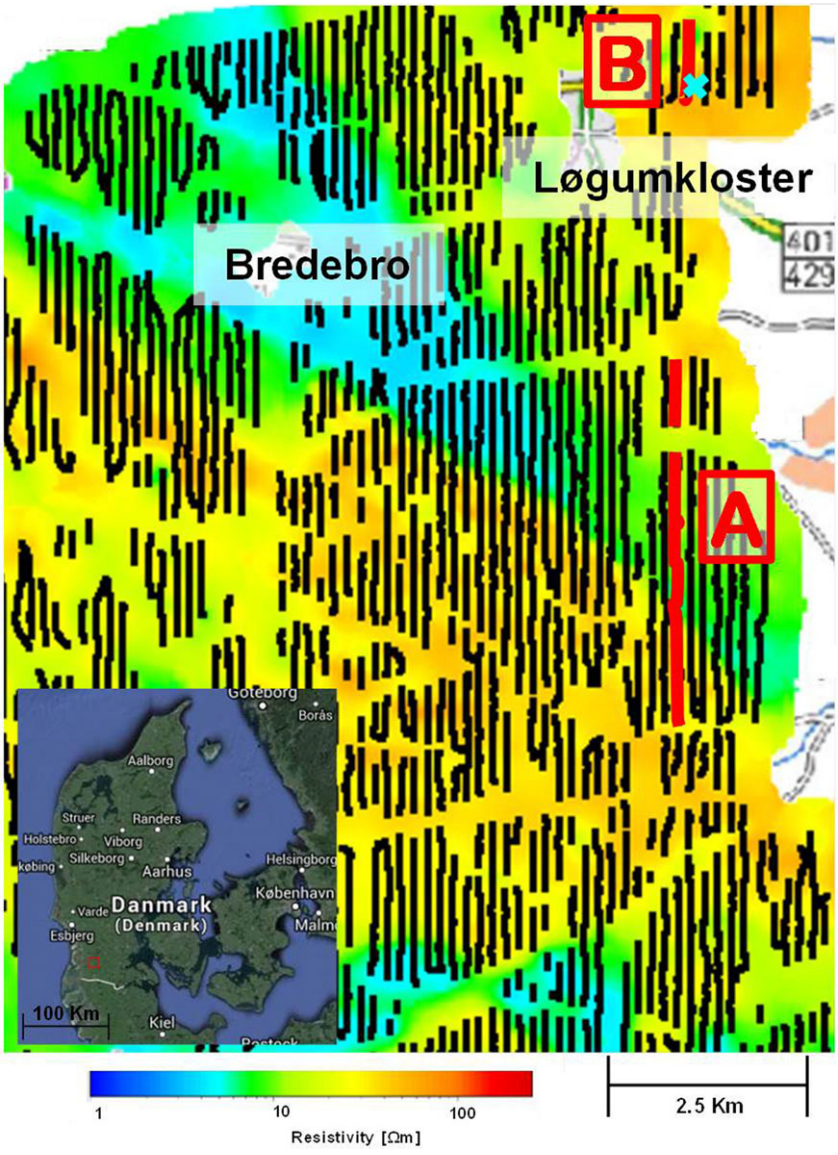

Figure 4 Map of the mean resistivity between -70 m and -80 m elevation of the survey area located near the border of Germany and Denmark. The sounding locations are shown in black (soundings characterized by capacitive/galvanic couplings and/or not optimal acquisition parameters have been removed). The two considered survey portions are highlighted in red: "A" indicates the section in Fig. 5, whereas "B" shows the section in Fig. 6. The blue cross mark near the "A" survey portion is the location of the borehole used for comparison in Fig. 6.

setting of the area, particularly by mapping buried valleys and salt–fresh water interfaces (Jørgensen *et al.* 2012). The data set was acquired using the SkyTEM system (Sørensen and Auken 2004) operating at an average speed of 43 km/h for a resulting averaged sounding every 25–30 m. Processing of the data was done using the methodology described in (Auken et al. 2009) and implemented in the Aarhus Workbench software package (www.aarhusgeophysics.com).

In order to best assess the differences between the sSCI and the SCI for actual field data, we show the results for two very characteristic cross sections: the first is characterized by sharp lateral and vertical variations in the resistivity distribution (probably a fault), the second is well suited for comparison due to the existence of high-quality borehole information close to the geophysical section.

Figures 5 and 6 show the results of the respective 30-layer SCI and sSCI inversions, all performed using the same settings as in the synthetic cases.

The geology of the area consists mainly of three sedimentary sequences: alternating Miocene sand, silt, and clay layers overlying Paleocene clay situated at a depth of about 300 m. The Miocene sequence is found below a shallow sheet of coarse glacial meltwater sediments and tills, which occasionally thickens when a buried valley is being filled. The

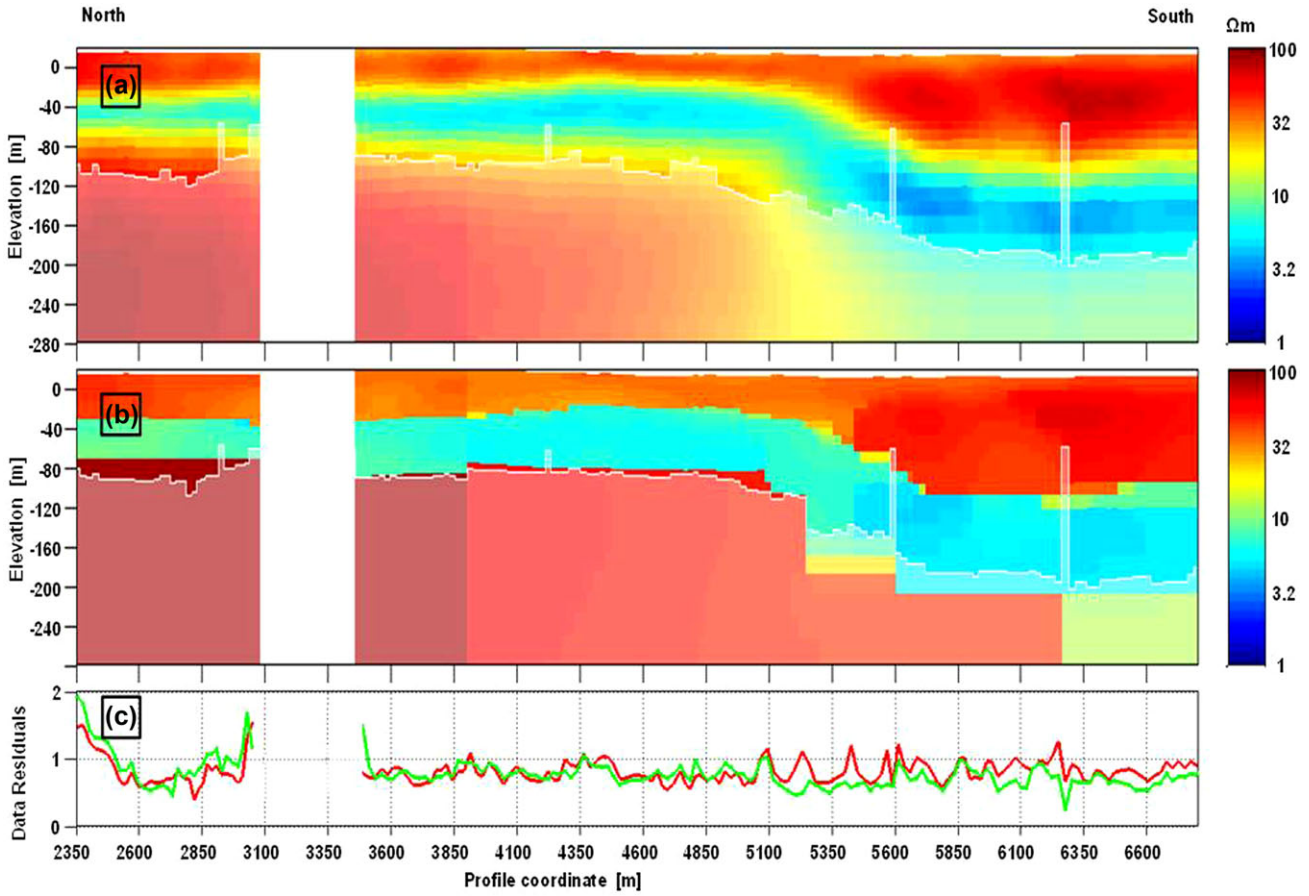

Figure 5 Southern cross section (section "A" in Fig. 4). (a) SCI. (b) sSCI. (c) Data misfit at each sounding location; the green and red lines represent the misfit of the SCI and the sSCI, respectively. The white-shaded area in (a) and (b) represents the DOI. Vertical exaggeration = 5.0x.

inversions of the first cross section are shown in Fig. 5. Both SCI and sSCI results achieve the same degree of data fit (Fig. 5(c)). In the southern part of the cross section, we find a fault located at around 5250 m, providing a very interesting target for comparison. Here, we see that the focusing regularization of the sSCI effectively eliminates the transition zone effects and provides a sharper and more realistic result. Along the entire section, in the smooth SCI inversion, we can notice two thin layers of slightly increased resistivity surrounding the conductive layer (Fig. 5(a)), whereas these layers do not exist in the focusing sSCI inversion (Fig. 5(b)). The sSCI solution of Fig. 5(b) provides (with a comparable data misfit) a much simpler picture characterized by a few very homogeneous zones that are much easier to interpret by a geologist. This prospect is of particular interest when looking towards future automated methods for relating geophysical and hydrological/lithological models (http://hgg.au.dk/projects/hygem/project-description/).

For the second field data example (Fig. 6), we compare the SCI and sSCI results against a borehole located just a few meters from the cross section (Fig. 4). By comparing the inversion results to ground truth, It is clear that the sSCI (Fig. 6(b)) is capable of reproducing the actual lithological transitions with higher precision than the smooth SCI. In particular, it is hard to tell from the smooth SCI whether there are two distinct layers above the Miocene clay or if this is just a single smeared out interface. In the sSCI case, two completely unambiguous layers are revealed, providing an almost perfect reconstruction of the interface between the top sand/gravel layer and the underlying clay. For the deeper lying layers, the sSCI again provides an excellent definition of the Miocene clay between −30 m and −52 m and its transition to a sandier lithology from −52 m down to the DOI. As a matter of fact, sSCI also appears successful in determining the sharp change to the sand layer situated immediately above the DOI (Fig. 6(b)).

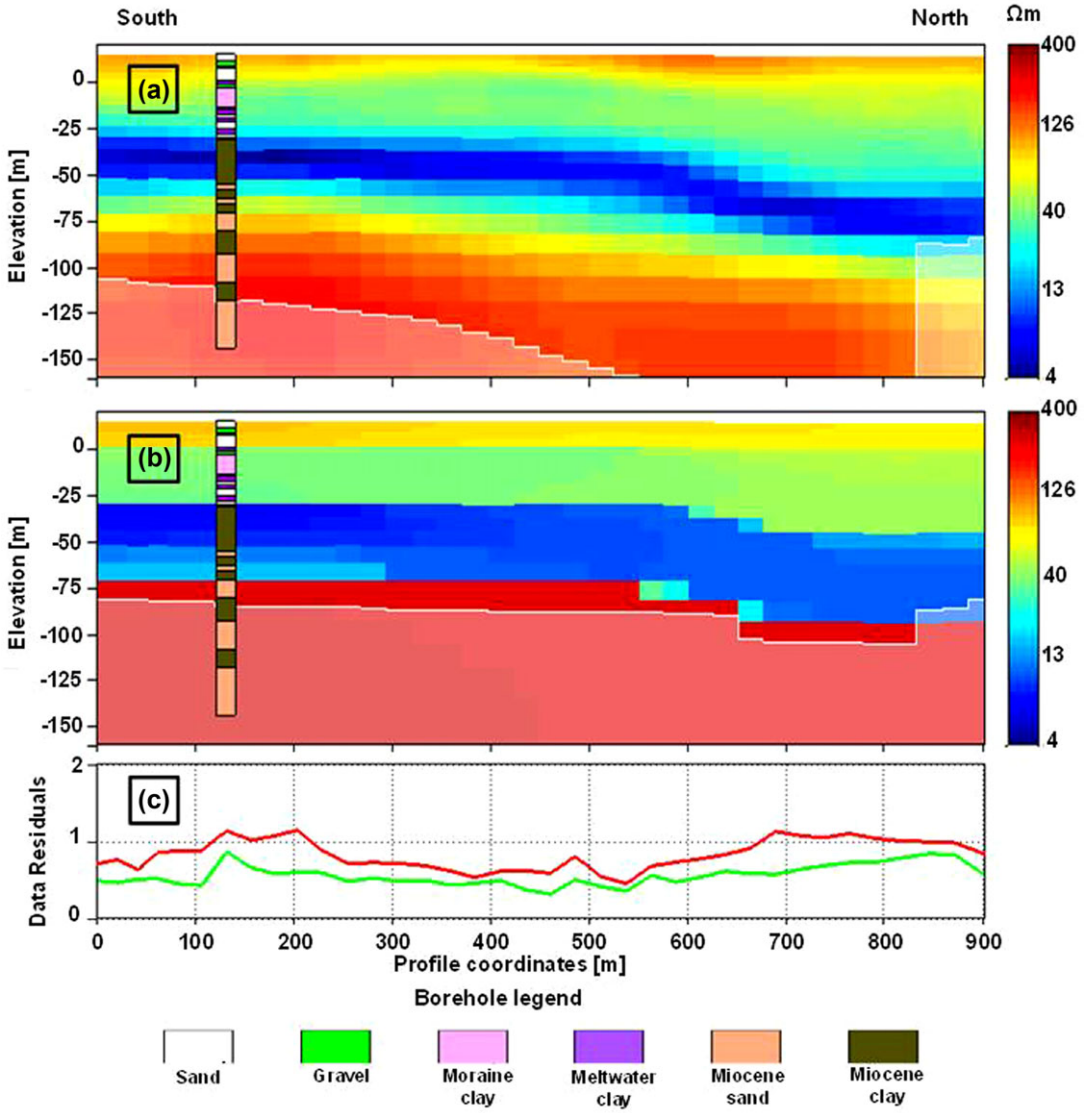

Figure 6 Northern cross section (section "B" in Fig. 4). (a) SCI and (b) sSCI resistivity results compared against the available borehole. (c) Data misfit at each sounding location; the green and red lines represent the misfit of the SCI and the sSCI, respectively. The white-shaded area in (a) and (b) represents the DOI. Vertical exaggeration = 1.8x.

5. CONCLUSIONS

In this paper, we have developed and applied an extension of the regularization used in the SCI scheme. The new sSCI algorithm implements an MGS stabilizer within the existing SCI framework: the original SCI (smoothing) regularization term is substituted by a new model-vector-dependent (focusing) stabilizing term. The MGS stabilizer allows the reconstruction of abrupt horizontal variations without the need for the discrete inversion with variable layer boundaries. The improved algorithm is very easy to be implemented and is proven to be effective on both synthetic and field TEM data sets. In particular, in the synthetic examples, we show how the sSCI compares to the traditional smooth and discrete SCI; the synthetic examples clearly demonstrate the sSCI superior capability to resolve sharp resistivity changes. In addition, in the case of actual field data, sSCI produces results that are much more geologically plausible and more homogeneous and retrieves more accurately the lithological information obtained from the available borehole.

Overall, we can draw the conclusion that, it is beneficial to employ a custom regularization scheme, such as sSCI, instead of simply utilizing one of the more widely known

smoothing stabilizers. Specifically, the sSCI provides the benefit of making no assumptions about a fixed number of layers in the ground, which is otherwise needed in order to resolve sharp resistivity variations by inverting for models with variable layer boundaries. Another useful feature of the sSCI approach is its ability to produce quasi-3D models consisting of subdomains with (quasi-)homogeneous resistivity. This capability could prove to be highly valuable for applications requiring models of minimum structure, e.g., automated geological interpretation schemes or integration with hydrological models.

The novel focusing algorithm is independent on the specific spatial derivative operator used. Thus, it can be coupled with no additional modifications to sophisticated $\mathbf{R}_p$ implementations. This might be useful, for example, any time the subsurface stratification does not follow the surface; in these cases, a derivative implementation that is taking into account not only the contributions from model parameters at the same depth but also contributions along the "diagonal" directions could prevent the layers to be incorrectly forced to follow the surface.

Concerning future applications, the algorithm is extremely general and flexible and can be easily applied to other data types. In fact, the presented sSCI scheme can be useful for any problem using a 1D forward model for the purpose of resolving sharp variations in either the horizontal or vertical direction. Examples of this could be: (i) the inversion of seismic surface wave data any time the dispersion curves are extracted via techniques preserving information about rapid lateral transition (Vignoli and Cassiani 2010; Vignoli *et al.* 2011) and (ii) application to the case of adjacent magnetic resonance soundings (Behroozmand *et al.* 2012a).

6. ACKNOWLEDGEMENTS

The authors would like to the World Bank and the Indian Government, Ministry of Water Resources, for their partial support to this research within the framework of the Aquifer Mapping (AQUIM) project (http://hgg.au.dk/projects/aquim/). In particular, they would like to thank Dr. Shakeel Ahmed and Dr. Subash Chandra from the National Geophysical Research Institute (CSIR-NGRI). They also thank the VILLUM center of excellence HOBE for their partial support. Moreover, the authors are grateful to the two anonymous reviewers for their valuable suggestions.

REFERENCES

Árnason K. 2008. *A Short Manual for the Program TEMDDD*. The National Energy Authority of Iceland, Reykjavík, Iceland.

Auken E. and Christiansen A.V. 2004. Layered and laterally constrained 2D inversion of resistivity data. *Geophysics* **69**, 752–761.

Auken E., Christiansen A.V., Jacobsen B.H., Foged N. and Sørensen K.I. 2005. Piecewise 1D laterally constrained inversion of resistivity data. *Geophysical Prospecting* **53**, 497–506.

Auken E., Christiansen A.V., Jacobsen L. and Sørensen K.I. 2008. A resolution study of buried valleys using laterally constrained inversion of TEM data. *Journal of Applied Geophysics* **65**, 10–20.

Auken E., Christiansen A.V., Westergaard J.A., Kirkegaard C., Foged N. and Viezzoli A. 2009. An integrated processing scheme for high-resolution airborne electromagnetic surveys, the SkyTEM system. *Exploration Geophysics* **40**, 184–192.

Behroozmand A.A., Auken E., Fiandaca G. and Christiansen A.V. 2012a. Improvement in MRS parameter estimation by joint and laterally constrained inversion of MRS and TEM data. *Geophysics* **74**, WB191–WB200.

Behroozmand A.A., Auken E., Fiandaca G., and Christiansen A.V. and Christensen N.B. 2012b. Efficient full decay inversion of MRS data with a stretched-exponential approximation of the inline image T_2^*distribution. *Geophysical Journal International* **190**, 900–912.

Blaschek R., Hördt A. and Kemna A. 2008. A new sensitivity-controlled focusing regularization scheme for the inversion of induced polarization data based on the minimum gradient support. *Geophysics* **73**, F45–F54.

Brodie R. 2010. *Holistic inversion of airborne electromagnetic data*. PhD thesis, The Australian National University, Australia.

Brodie R. and Sambridge M. 2006. A holistic approach to inversion of frequency-domain airborne EM data. *Geophysics* **71**, G301–G312.

Christensen N.B. and Tølbøll R.J. 2009. A lateral model parameter correlation procedure for one-dimensional inverse modelling. *Geophysical Prospecting* **57**, 919–929.

Christiansen A.V. and Auken E. 2012. A global measure for depth of investigation. *Geophysics* **77**, WB171–WB177.

Constable S.C., Parker R.L. and Constable C.G. 1987. Occam's inversion: a practical algorithm for generating smooth models from electromagnetic sounding data. *Geophysics* **52**, 289–300.

Cox L.H., Wilson G.A. and Zhdanov M.S. 2010. 3D inversion of airborne electromagnetic data using a moving footprint. *Exploration Geophysics* **41**, 250–259.

Fiandaca G., Auken E., Gazoty A. and Christiansen A.V. 2012. Time-domain induced polarization: full-decay forward modeling and 1D laterally constrained inversion of Cole-Cole parameters. *Geophysics* **77**, E213–E225.

Fiandaca G., Ramm J., Binley A., Gazoty A., Christiansen A.V. and Auken E. 2013. Resolving spectral information from time domain induced polarization data through 2-D inversion. *Geophysical Journal International* **192**, 631–646.

Guillemoteau J., Sailhac P. and Behaegel M. 2012. Fast approximate 2D inversion of airborne TEM data: Born approximation and empirical approach. *Geophysics* **77**, WB89–WB97.

Haber E., Oldenburg D.W. and Shekhtman R. 2007. Inversion of time domain three-dimensional electromagnetic data. *Geophysical Journal International* **171**, 550–564.

Harbo M.S., Pedersen J., Johnsen R. and Petersen K. 2011.*Groundwater in a Future Climate*. ISBN: 87–7788–265–2

Jørgensen F., Scheer W., Thomson S., Sonnenborg T.O., Hinsby K., Wiederhold H. *et al*. 2012. Transboundary geophysical mapping of geological elements and salinity distribution critical for the assessment of future sea water intrusion in response to sea level rise. *Hydrology and Earth System Sciences* **16**, 1845–1862.

Marquart D. 1963. An algorithm for least squares estimation of nonlinear parameters. *SIAM Journal of Applied Mathematics* **11**, 431–441.

Monteiro Santos F.A. 2004. 1-D laterally constrained inversion of EM34 profiling data. *Journal of Applied Geophysics* **56**, 123–134.

Newman G. and Commer M. 2005. New advances in three dimensional transient electromagnetic inversion. *Geophysical Journal International* **160**, 5–32.

Newman G.A., Anderson W.L. and Hohmann G.W. 1987. Interpretation of transient electromagnetic soundings over three-dimensional structures for the central-loop configuration. *Geophysical Journal of The Royal Astronomical Society* **89**, 889–914.

Pagliara G. and Vignoli G. 2006. Focusing inversion techniques applied to electrical resistance tomography in an experimental tank. *International Association for Mathematical Geology XI International Congress Processing*.

Portniaguine O. and Zhdanov M.S. 1999. Focusing geophysical inversion images. *Geophysics* **64**, 874–887.

Sasaki Y. 2001. Full 3-D inversion of electromagnetic data on PC. *Journal of Applied Geophysics* **46**, 45–54.

Sasaki Y.N.H. 2003. Topographic effects in frequency-domain helicopterborne electromagnetics. *Exploration Geophysics* **34**, 24–28.

Sengpiel K.P. and Siemon B. 2000. Advanced inversion methods for airborne electromagnetic exploration. *Geophysics* **65**, 1983–1992.

Sørensen K.I. and Auken E. 2004. SkyTEM – A new high-resolution helicopter transient electromagnetic system. *Exploration Geophysics* **35**, 191–199.

Tikhonov A.N. and Arsenin Y.V. 1977. *Solution of Ill-Posed Problems*. Winston & Sons. ISBN 0–470–99124–0.

Triantafilis J. and Monteiro Santos F.A. 2009. 2-dimensional soil and vadose zone representation using an EM38 and EM34 and a laterally constrained inversion model. *Australian Journal of Soil Research* **47**, 809–820.

Vallée M.A. and Smith R.S. 2009. Inversion of airborne time-domain electromagnetic data to a 1D structure using lateral constraints. *Near Surface Geophysics* **7**, 63–71.

Viezzoli A., Christiansen A.V., Auken E. and Sørensen K.I. 2008. Quasi-3D modeling of airborne TEM data by spatially constrained inversion. *Geophysics* **73**, F105–F113.

Viezzoli A., Munday T., Auken E. and Christiansen A.V. 2010. Accurate quasi 3D versus practical full 3D inversion of AEM data – the Bookpurnong case study. *Preview* **149**, 23–31.

Vignoli G. and Cassiani G. 2010. Identification of lateral discontinuities via multi-offset phase analysis of surface wave data. *Geophysical Prospecting* **58**, 389–413.

Vignoli G., Cassiani G. and Deiana R. 2012. Focused inversion of vertical radar profile (VRP) traveltime data. *Geophysics* **77**, H9–H18.

Vignoli G., Strobbia C., Cassiani G. and Vermeer P. 2011. Statistical multi-offset phase analysis (sMOPA) for surface wave processing in laterally varying media. *Geophysics* **76**, U1–U11.

Wilson G.A., Raiche A. and Sugeng F. 2006. 2.5D inversion of airborne electromagnetic data. *Exploration Geophysics* **37**, 363–371.

Wisén R. and Christiansen A.V. 2005. Laterally and mutually constrained inversion of surface wave seismic data and resistivity data. *Journal of Environmental & Engineering Geophysics* **10**, 251–262.

Yang D. and Oldenburg D.W. 2012. Three-dimensional inversion of airborne time-domain electromagnetic data with applications to a porphyry deposit. *Geophysics* **77**, B23–B34.

Zhdanov M.S. 2002. Geophysical inverse theory and regularization problems. *Elsevier*. ISBN-10: 0–444–51089–3.

Zhdanov M.S. and Tolstaya E. 2004. Minimum support nonlinear parametrization in the solution of a 3D magnetotelluric inverse problem. *Inverse Problems* **20**, 937–952.

Zhdanov M.S., Vignoli G. and Ueda T. 2006. Sharp boundary inversion in crosswell traveltime tomography. *Journal of Geophysics and Engineering* **3**, 122–134.